Marine and Petroleum Geology 120 (2020) 104565

Contents lists available at ScienceDirect

Marine and Petroleum Geology

journal homepage: www.elsevier.com/locate/marpetgeo

Research paper

Methane adsorption characteristics of overmature Lower Cambrian shales of deepwater shelf facies in Southwest China

Haifeng Gai [a], Tengfei Li [a], Xing Wang [a,b], Hui Tian [a,*], Xianming Xiao [c], Qin Zhou [a]

[a] State Key Laboratory of Organic Geochemistry, Guangzhou Institute of Geochemistry, Chinese Academy of Sciences, Guangzhou, 510640, China
[b] University of Chinese Academy of Science, Beijing, 100049, China
[c] School of Energy Resources, China University of Geosciences, Beijing, 100083, China

ARTICLE INFO

Keywords:
shale gas
methane adsorption
Lower Cambrian shale
Southwest China

ABSTRACT

The Lower Cambrian shales of deepwater shelf facies comprise an important part of the marine black shales in southern China. In this study, twenty-four Lower Cambrian shale samples from southwest China were subjected to analysis of geochemistry, pore structure and methane adsorption capacity. The samples have total organic carbon (TOC) contents ranging from 0.25% to 11.3% and equivalent vitrinite reflectance (EqVRo) values in the range of 2.51–4.23%. Specific surface areas determined from N_2 adsorption at 77.4 K and specific micropore volumes from CO_2 adsorption at 273.15 K are in the range of 3.0–38.6 m^2/g rock and 2.5–11.4 cm^3/kg rock, respectively, and both of them have positive relationships with TOC values. The Langmuir volumes of these samples at 60 °C range from 0.47 cm^3/g rock to 5.96 cm^3/g rock and are positively correlated with TOC values, which on the one hand confirms the TOC control on methane adsorption capacity and on the other hand also suggests a weak control of thermal maturity on methane adsorption capacity at overmature stages. Although both specific surface area and specific micropore volume are positively correlated with methane adsorption capacity, the latter seems to have a stronger effect and the specific micropore volume determined from subcritical CO_2 adsorption may be considered as a proxy for the volume of adsorbed methane in dry shales. For the extrapolation of measured methane excess adsorption isotherms to geological conditions, the use of a constant or varying Langmuir volume makes no significant difference with respect to the methane storage capacity of shales when the density of the adsorbed methane is allowed to change with temperature. However, the absolute methane adsorption quantity at subsurface is obviously dependent on the use of a constant or varying Langmuir volume, which subsequently affects the estimation of the relative percentages of adsorbed and free methane.

1. Introduction

Unlike the conventional gas reservoirs where gas is mainly stored in a free state, the gas in shale reservoirs may be present in free, adsorbed and absorbed states (Curtis, 2002; Montgomery et al., 2005) because gas shales usually hold complex organic and/or inorganic nano-scale pore networks that provide larger surface areas for gas adsorption than μm-scale pore systems in conventional reservoirs (Chalmers and Bustin, 2007; Loucks et al., 2009; Bernard et al., 2012; Milliken et al., 2013; Mastalerz et al., 2013; Furmann et al., 2014; Tian et al., 2015). Depending on geochemical and geological conditions, adsorbed gas may accounts for 20–85% of total gas content of a shale (Curtis, 2002; Jarvie, 2012). In particular, many gas shales have experienced tectonic uplifting and subsequent temperature and pressure declines, which usually leads to an increased percentage of adsorbed gas in shallower depths (Rexer et al., 2013; Bruns et al., 2016; Pan et al., 2016, and references therein).

As a bulk geochemical parameter of shales, total organic carbon (TOC) content is usually considered as a main control on methane adsorption capacity (Chalmers and Bustin, 2007; Ross and Bustin, 2009; Weniger et al., 2010; Rexer et al., 2014; Tian et al., 2016; Topór et al., 2017); however, there are some exceptions where methane adsorption capacity is negatively correlated to TOC but positively to the content of total clays for organic-lean samples (Gasparik et al., 2012), indicating that clay minerals may also play a role in methane adsorption when they are free of moisture (Ji et al., 2012; Jin and Firoozabadi, 2014). From the perspective of nanopore networks in shales, gas adsorption capacity is

* Corresponding author. #511 Kehua Road, Tianhe District, Guangzhou City, Guangdong Province, China.
E-mail address: tianhui@gig.ac.cn (H. Tian).

https://doi.org/10.1016/j.marpetgeo.2020.104565
Received 23 March 2020; Received in revised form 22 June 2020; Accepted 28 June 2020
Available online 7 July 2020

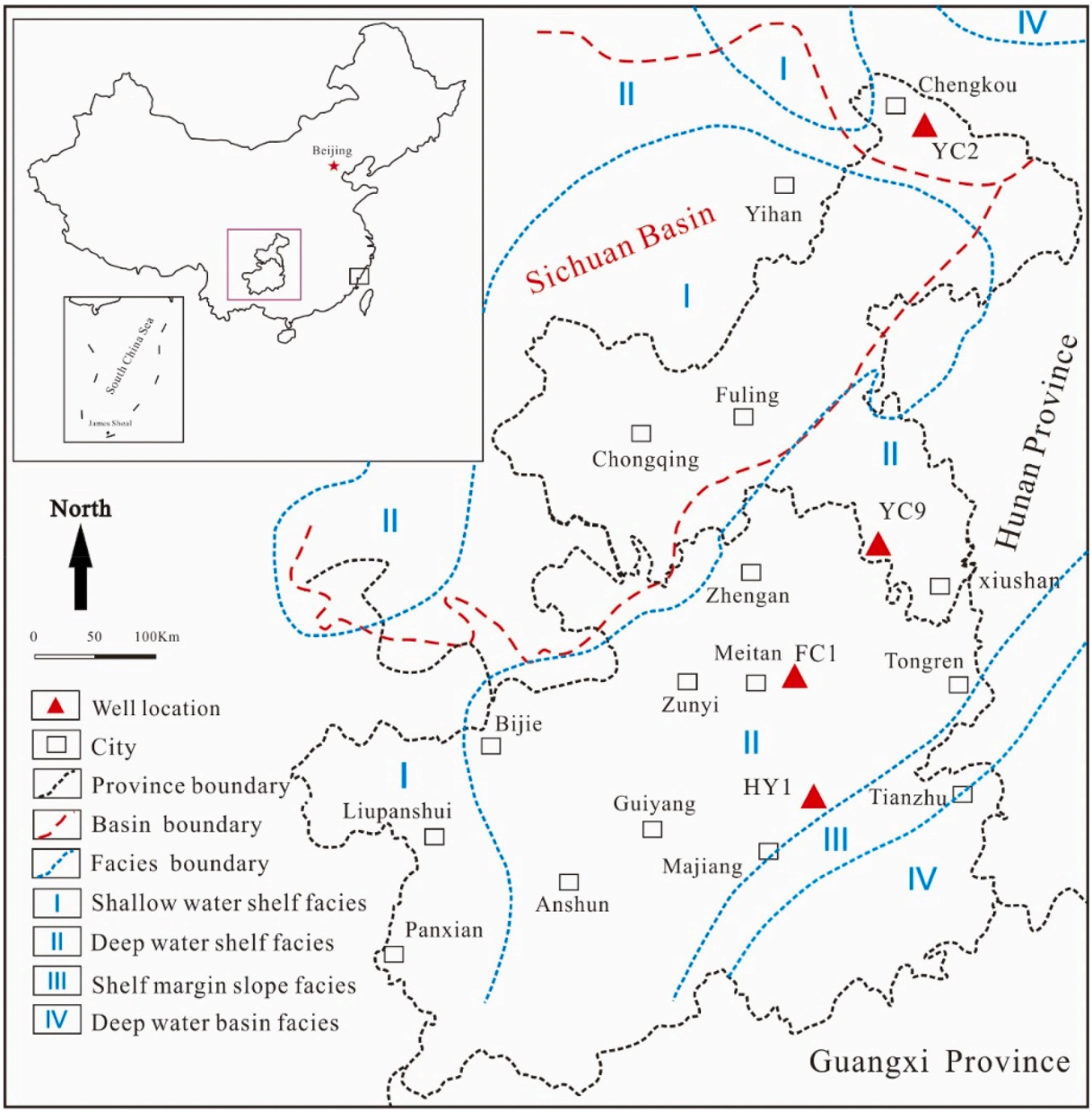

Fig. 1. Schematic map showing sampling locations (modified from Li et al., 2017; Liu et al., 2017).

usually positively related to specific micropore volume (e.g., Ross and Bustin, 2009) because gas adsorption potentials in micropores (<2 nm in diameter) are stronger than in larger pores (Mosher et al., 2013; Rexer et al., 2014). In general, organic matter is considered to be favorable for the formation of micropores in shales (Ross and Bustin, 2009; Bernard et al., 2012; Tian et al., 2015; Topór et al., 2017), which explains the positive correlation between TOC and methane adsorption capacity of mature shales. Nevertheless, there are some cases where no or very weak correlations between TOC and specific micropore volume are observed for some shales, indicating contribution of clay minerals to micropores (Ross and Bustin, 2009; Sander et al., 2018). More interestingly, Weishauptová et al. (2017) reported that methane adsorption capacities for some Czech Silurian shales are negatively correlated to their specific micropore volumes, but they do show a positive relationship with the relative percentages of micropore volume, which is very confusing but not explained by the authors.

It is also worthy to note that there are some disagreements about the thermal maturity effect on gas adsorption behavior of shales. Some authors believe that higher thermal maturity enhances the formation of micropores and hence promotes gas adsorption capacity, especially for shales with Ro values smaller than 2.0% (Ross and Bustin, 2009; Gasparik et al., 2014), while others documented only a minor enhancement of gas adsorption capacity at elevated thermal maturity (Gasparik et al., 2012; Zhang et al., 2012). This may indicate that the thermal maturity alone cannot determine the pore formation and subsequent gas adsorption capacity of shales, and other controls have to be considered (Curtis et al., 2012; Fishman et al., 2012). In addition, very high thermal maturity levels (e.g., Ro > 3.5–4.0%) may somehow cause a lower gas adsorption capacity (Gasparik et al., 2014; Li et al., 2017; Topór et al., 2017) because the micropores are destroyed at such high thermal maturity stages (Chen and Xiao, 2014). Nevertheless, there is a general agreement about a decrease of the Langmuir pressure at higher thermal maturity levels, indicating that the adsorbed gas may become more difficult to desorb at subsurface (Zhang et al., 2012; Gasparik et al., 2014).

Commercial shale gas production from the Lower Silurian Longmaxi

Table 1
Total organic carbon (TOC), bitumen reflectance (BRo), mineralogical compositions, specific surface areas (S_{BET}) calculated from N_2 adsorption isotherms at 77.4 K with BET equation and specific micropore volumes (V_{DR}) determined from CO_2 adsorption isotherms at 273.15 K with Dubinin–Radushkevich (DR) equation.

Well	Sample	Fm	Depth (m)	TOC (%)	[a]Mean BRo (%)	S_{BET} (m^2/g)	V_{DR} (cm^3/kg)	XRD mineralogical composition (%)				
								quartz	feldspar	carbonate	total clays	pyrite
YC9	YC9-2	Niutitang	1369.83	0.75	n.d.	4.9	2.5	23.5	11.6	0.0	62.8	1.3
	YC9-5		1410.85	0.25	n.d.	3.0	2.7	22.1	11.0	13.0	51.8	1.9
	YC9-8		1414.53	4.28	n.d.	14.4	6.4	24.3	15.4	5.6	48.9	1.5
	YC9-10		1428.51	3.34	n.d.	9.9	5.2	35.0	15.8	10.5	32.3	3.1
	YC9-13		1439.93	2.02	4.20	9.2	3.3	39.1	18.4	5.9	31.4	3.2
	YC9-15		1447.75	4.53	n.d.	13.3	7.7	36.4	20.3	7.1	25.0	6.7
	YC9-17		1452.93	7.17	4.14	15.9	9.0	68.3	4.6	5.3	11.8	2.7
	YC9-18		1454.55	8.52	n.d.	15.8	8.8	64.9	5.2	0.0	18.7	2.7
YC2	YC2-2	Shuijingtuo	956.56	3.16	n.d.	8.0	4.8	35.9	15.4	11.1	31.8	2.5
	YC2-5		1023.77	1.90	n.d.	3.6	3.2	27.1	20.4	5.3	39.0	6.3
	YC2-8		1078.83	4.53	2.63	11.0	4.4	25.8	22.1	29.9	16.2	1.4
	YC2-9		1086.86	2.53	2.41	5.4	4.2	29.4	15.9	27.0	23.1	2.1
	YC2-13		1115.6	1.87	2.63	3.4	2.6	32.1	18.9	9.0	32.9	5.1
	YC2-14		1130.83	2.47	2.67	7.2	3.9	29.2	13.1	12.5	40.8	2.0
	YC2-16		1147.62	1.37	2.82	5.2	2.9	27.6	22.1	11.5	35.5	1.9
HY1	HY-1	Jiumenchong	2371.01	10.50	*3.06*	35.0	11.2	36.1	8.2	0.9	41.9	2.4
	HY-2		2373.80	11.20	*3.01*	38.6	11.4	29.9	8.4	3.8	44.8	2.0
	HY-3		2380.05	5.50	*3.10*	22.8	7.4	29.0	9.8	5.8	46.1	4.0
	HY-4		2384.90	6.20	*2.82*	23.8	7.7	32.9	15.5	4.7	36.7	4.0
	HY-5		2389.30	3.40	*2.82*	19.3	6.1	31.2	17.2	11.8	32.5	4.1
	HY-6		2396.45	4.70	*3.02*	22.1	8.6	38.3	16.9	0.5	36.0	3.6
	HY-7		2401.55	7.20	*3.17*	27.2	8.4	33.1	13.5	3.2	40.4	2.6
	HY-8		2407.32	6.80	*n.d.*	26.2	9.0	32.2	15.9	4.6	38.3	2.2
	HY1-9		2415.04	5.70	*3.04*	19.7	7.7	33.4	15.8	0.0	39.9	5.2

[a] BRo values for samples from Well HY1 is cited from Tian et al. (2015) whose samples are contiguous to the present samples. n.d. = not determined.

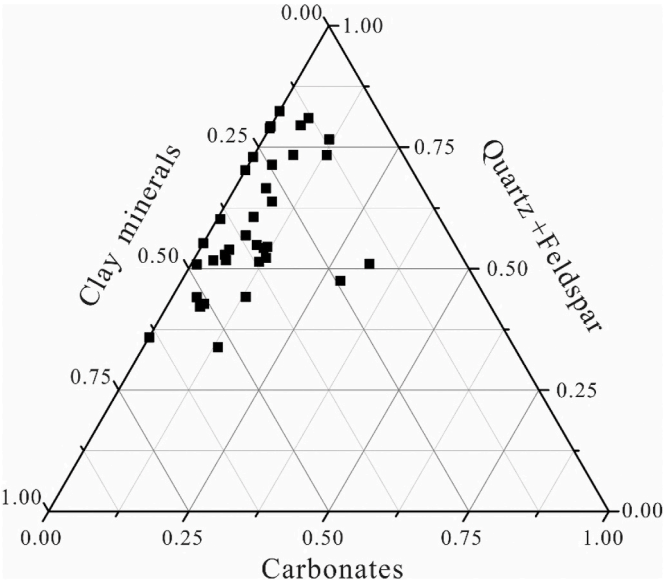

Fig. 2. Ternary plot showing the relative mineral compositions for our samples.

shale has recently been achieved in southern China (Guo, 2013; Guo and Zhang, 2014), and many relevant studies have been conducted on this set of shale (Chen et al., 2011; Tian et al., 2013; Wang et al., 2013a; Tan et al., 2014a, b; Dai et al., 2016, and references therein). However, only little commercial achievements have been made on the Lower Cambrian shales, although they are more widely distributed and usually have greater thickness of organic-rich layers than the Lower Silurian shales (Nie et al., 2011; Hao et al., 2013; Tan et al., 2014b; Li et al., 2017). The poor success rate in developing the Lower Cambrian shale gas plays is probably related to their very high thermal maturity levels that correspond to a deep burial and strong mechanical compaction in geological history and thus a significant reduction of porosity and permeability (Wang et al., 2013a; Tian et al., 2015). In recent years, some studies have been conducted on the methane adsorption capacity of Lower Cambrian shale samples at various temperature and pressure ranges (Han et al., 2013; Tan et al., 2014b; Ma et al., 2015; Sun et al., 2015; Han et al., 2016; Yang et al., 2015; Li et al., 2016). Li et al. (2017) also carried out a series of methane isothermal adsorption experiments under pressures up to 35 MPa on Lower Cambrian shale samples with Ro values of approximately 4.0% and found that the methane adsorption capacity of organic matter in these shale samples is somehow slightly reduced compared with other shales of relatively low thermal maturity. These results are similar to those of Gasparik et al. (2014) in their samples with very high thermal maturity.

In this study, twenty four overmature Lower Cambrian shale core samples were collected from three wells in southern China. In general, overmaturity corresponds to Ro values greater than 1.35%, including hydrocarbon gas generation stages of both wet gas (Ro = 1.35–2.0%) and dry gas (Ro>2.0%) (e.g., Mastalerz et al., 2013). In particular, the overmaturity discussed here denotes the dry gas stage (Ro>2.0%, Littke et al., 1999). All the samples were analyzed with respect to their pore structures and methane adsorption capacity through subcritical N_2 and CO_2 gas adsorption and supercritical methane adsorption experiments, respectively. Based on these analyses, their methane adsorption characteristics and main controls at overmature stage (Ro>2.0% in this study) were discussed. The results may provide some new insights into the evaluation of Lower Cambrian shale gas in southern China and other similar shales around the world.

2. Samples and methods

2.1. Samples

Twenty four marine black shale core samples of the Early Cambrian age were collected from three wells in the Chongqing and Guizhou regions in southwest China, and they were all formed in depositional environments of deepwater shelf facies (Fig. 1, Table 1). The study area is presently a part of the Upper Yangtze block where the Lower Cambrian black shales are widely distributed with thickness ranging from 20 m to 200 m (Wang et al., 2012, 2013b; Liu et al., 2017). With marine transgression in the Early Cambrian, this set of black shales was formed under

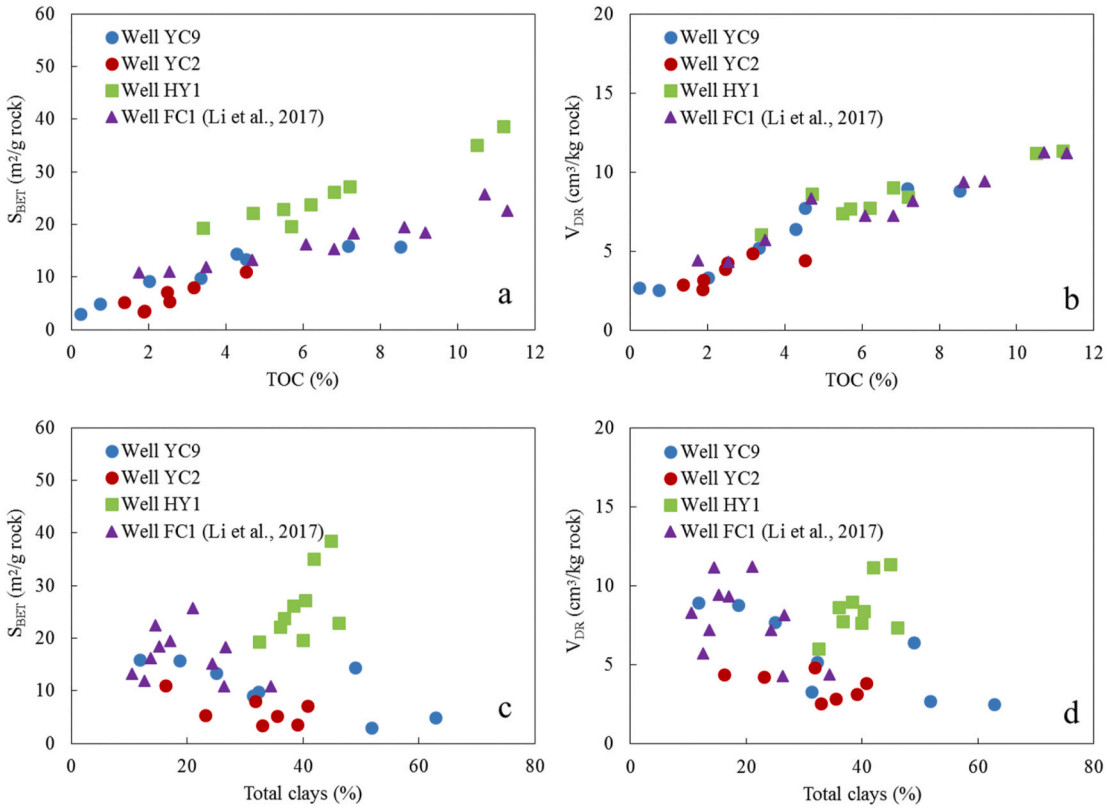

Fig. 3. Plots showing the relationships between TOC and (a) specific surface area (S_{BET}) and (b) specific micropore volume (V_{DR}), and the relationships between total clays and (c) specific surface area (S_{BET}) and (d) specific micropore volume (V_{DR}).

continental shelf environments with water deepening from northwest to southeast (Wang et al., 2013b; Bai et al., 2015; Liu et al., 2017). The local names for this set of black shales are different in different regions. For example, it is usually named as the Niutitang Formation in regions from central Guizhou to southeastern Chongqing (wells FC1 and YC9), Jiumenchong Formation in southern Guizhou (Well HY1), and Shuijingtuo Formation in northeastern Chognqing (Well YC2; Liu et al., 2017). During late Yanshanian through Himalayan orogenies, the Paleozoic to Mesozoic strata were eroded to various extents in the study area and the Lower Cambrian shales have been even uplifted to the surface in certain places (Wang et al., 2013b; Leng et al., 2016; Liu et al., 2017).

2.2. TOC and XRD mineralogical compositions

TOC measurements were conducted on carbonate-free samples using a carbon/sulfur analyzer LECO CS-200. Whole rock samples were ground to grains smaller than 70 μm in size and then analyzed using a Bruker D8 ADVANCE X-ray diffractometer. The semi-quantitative compositions of minerals were determined following the method of Chalmers and Bustin (2008). Due to the absence of vitrinite in Lower Cambrian shales, pyrobitumen reflectance (BRo) was measured under oil immersion on one-side polished whole rock blocks to characterize the thermal maturity levels of our samples (Tian et al., 2013).

2.3. Subcritical N_2 and CO_2 gas adsorption

Depending on the TOC content, approximate 1–2 g of each sample whose grain sizes range from 300 to 750 μm in diameter were used for subcritical N_2 adsorption at 77.4 K and CO_2 adsorption at 273.15 K on a Micromeritics ASAP 2020^M apparatus. For N_2 adsorption, both adsorption and desorption isotherms were obtained, covering a relative pressure (p/p_0) range of 0.0009–0.995; for CO_2 adsorption, only adsorption isotherms were acquired with relative pressures (p/p_0) ranging from 0.00001 to 0.032. During experiments, the gas adsorption equilibrium time was set to be 30 s for both N_2 and CO_2 adsorption. Following the method of Rouquerol et al. (2007), a suitable p/p_0 range from N_2 adsorption isotherm was chosen to calculate the specific surface area (S_{BET}) with the BET equation (Brunauer et al., 1938); specific micropore volumes (V_{DR}, the volume of pores of less than 2 nm in diameter) were calculated from the CO_2 adsorption isotherms with the Dubinin–Radushkevich (DR) equation (Gregg and Sing, 1982).

2.4. Supercritical methane excess adsorption and parametrization

A commercial gas adsorption setup (ISOSORP-HP Static II model) manufactured by Rubotherm GmbH, Germany was used to collect the methane excess adsorption isotherms (n_{excess}). The measuring principles and procedures of this setup have been well illustrated in literature (Dreisbach and Lösch, 2002; De Weireld et al., 1999; Pan et al., 2016; Li et al., 2017). In this study, methane excess adsorption measurements at 60 °C under pressures up to 35 MPa were conducted on all samples. Three samples from Well HY1 were selected for further investigation of methane adsorption capacity at other temperatures (40, 80, 100, and 120 °C). To reduce the grain size effect as much as possible for the comparison between pore structure and methane adsorption capacity, the sample grain sizes used for methane excess adsorption experiments are the same as those used for subcritical N_2 and CO_2 adsorption experiments.

The measured methane excess adsorption isotherms were approximated with the Langmuir-based excess adsorption function (Krooss et al., 2002; Gasparik et al., 2014; Gensterblum et al., 2013; Tian et al., 2016), which is written as Eq. (1):

$$n_{excess} = n_{\infty} \cdot \frac{K_L \cdot P}{1 + K_L \cdot P} \cdot \left(1 - \frac{\rho_g}{\rho_{ads}}\right) \quad (1)$$

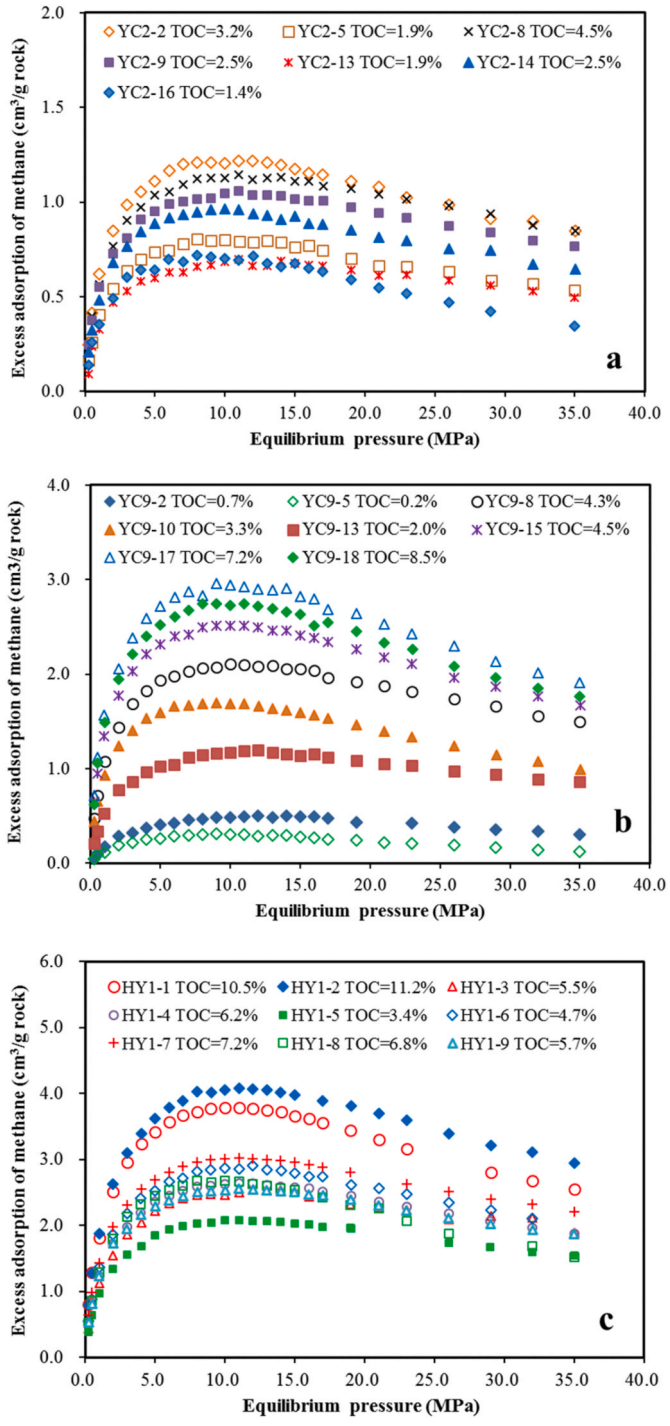

Fig. 4. Plots showing methane excess adsorption isotherms measured at 60 °C for samples from wells YC2 (a), YC9 (b) and HY1 (c).

where K_L is the Langmuir constant at given temperature, MPa^{-1}; n_∞ is the Langmuir volume at infinite pressure and expressed as cm^3/g rock under standard temperature and pressure (0 °C and 101.325 kPa, NIST); ρ_{ads} is the adsorbed phase methane density, mg/cm^3; ρ_g denotes the density of methane in the free state, mg/cm^3; P is the equilibrium pressure for methane adsorption, MPa. The adsorption parameters were first estimated by assuming an adsorbed methane density of 424 mg/cm^3, the density of liquid methane at its boiling point (Rexer et al., 2013; Gasparik et al., 2014), and then were optimized using a least-squares minimization procedure (Gasparik et al., 2014).

Table 2
Maxima of measured methane excess adsorption (M_{excess}) and freely fitted adsorption parameters using the Langmuir-based excess adsorption model.

[a]Sample	M_{excess} (cm^3/g rock)	[b]n_∞ (cm^3/g)	K_L (1/MPa)	ρ_{ads} (mg/cm^3)
YC9-2	0.49	0.88	0.22	333
YC9-5	0.31	0.53	0.28	267
YC9-8	2.10	2.83	0.58	468
YC9-10	1.69	2.33	0.65	372
YC9-13	1.19	1.68	0.42	450
YC9-15	2.51	3.39	0.63	430
YC9-17	2.96	4.00	0.61	415
YC9-18	2.75	3.73	0.62	408
YC2-2	1.22	1.66	0.58	443
YC2-5	0.80	1.11	0.54	411
YC2-8	1.14	1.50	0.59	523
YC2-9	1.06	1.37	0.62	508
YC2-13	0.70	0.91	0.55	515
YC2-14	0.96	1.30	0.59	429
YC2-16	0.71	1.06	0.49	313
HY-1	3.79	5.60	0.40	392
HY-2	4.08	5.66	0.48	465
HY-3	2.54	3.61	0.40	442
HY-4	2.69	3.70	0.47	451
HY-5	2.22	2.89	0.46	475
HY-6	2.87	4.00	0.47	457
HY-7	3.02	4.36	0.39	432
HY-8	2.95	4.12	0.43	346
HY1-9	2.56	3.74	0.39	438
FC1-37	1.41	2.01	0.40	377
FC1-38	1.39	1.90	0.45	266
FC1-45	2.49	3.60	0.47	397
FC1-47	1.78	2.52	0.62	344
FC1-49	2.69	3.62	0.68	480
FC1-53	4.15	5.85	0.54	386
FC1-55	3.46	4.55	0.58	541
FC1-59	3.52	4.69	0.60	457
FC1-62	2.53	3.75	0.48	316
FC1-66	2.93	4.16	0.45	420
FC1-72	3.97	5.44	0.51	444

[a] Adsorption data for samples from Well FC1 (in italic font) are adopted from Li et al. (2017).

[b] 1 mmol/g rock = 16 mg/g rock, which corresponds to 22.4 cm^3/g rock at the standard temperature (0 °C) and pressure (101.325 kPa) following the definition of National Institute of Standards and Technology (NIST).

3. Results

3.1. TOC, mineralogical compositions and pore structures

As shown in Table 1, the TOC values for samples from Well YC9 range from 0.25% to 8.52%; from 1.37% to 4.53% for samples from Well YC2, and from 3.40% to 11.20% for samples from Well HY1. Mean reflectance values measured on pyrobitumen grains (BRo) vary from 2.41% to 4.20% (Table 1). Generally, samples from Well YC9 display high BRo values whereas samples from Well YC2 have low BRo values, and the inconsistency between the BRo values and present burial depths indicate that the three wells have undergone different burial and uplift histories. To convert the measured BRo values to equivalent vitrinite reflectance (EqVRo) values, the equation of EqVRo=(BRo+0.2443)/1.0495 by Schoenherr et al. (2007) was adopted, and the investigated samples have EqVRo values in the range of 2.53–4.23%, indicating they are all overmature and have reached the late or end stage of hydrocarbon gas generation (Littke et al., 1999).

Mineralogical compositions for the 24 samples are summarized in Table 1 and presented in Fig. 2. Significant variations in mineralogical compositions are present among samples from different wells or even a single well, indicating that the shales are very heterogeneous with respect to their compositions (Chalmers and Bustin, 2017). For most samples, quartz and feldspar minerals account for 33–73% of the whole rocks, with half of them greater than 50%; carbonate contents vary from below detection to 29.9%, and the highest carbonate contents are

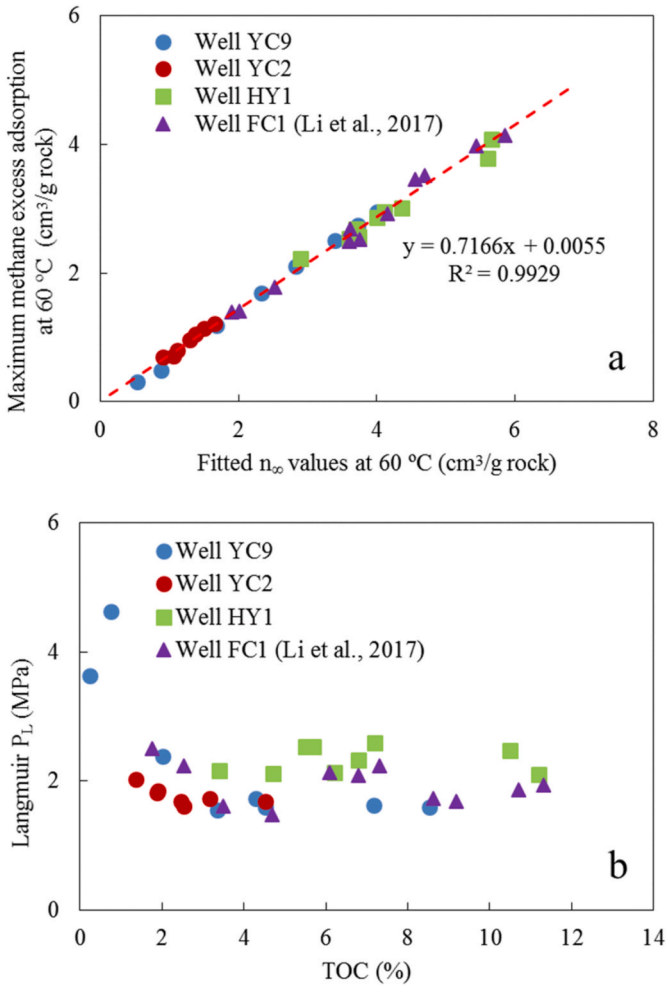

Fig. 5. Plots showing the relationship between measured maximum methane excess adsorption capacity (M_{excess}) and fitted Langmuir volume (n_∞) (a) and the relationship between Langmuir pressure (P_L) and TOC (b).

observed in samples from Well YC2 (Table 1); total clay contents also vary significantly among samples, ranging from 10% to 63%; various contents of pyrite are observed in the range of 1.3–6.7%, and the wide occurrence of fine framboidic pyrite suggests that these shales were formed in a reducing depositional environment (Wignall and Newton, 1998).

The specific surface areas (S_{BET}) and micropore volumes (V_{DR}) for our 24 samples are also summarized in Table 1. The S_{BET} values are in the range of 3.0–38.6 m^2/g rock, and are largely positively correlated with the TOC values (Fig. 3a); V_{DR} values range from 2.5 cm^3/kg rock to 11.4 cm^3/kg rock and also display a positive correlation with TOC values (Fig. 3b). By contrast, the relationships between total clays and S_{BET} and V_{DR} values are complex and seem to be different for different wells (Fig. 3c and d), which indicates that their contribution to S_{BET} and V_{DR} is probably masked by organic matter (Ross and Bustin, 2009; Furmann et al., 2014; Topór et al., 2017).

3.2. Methane adsorption at 60 °C

The methane excess adsorption isotherms measured at 60 °C for our 24 samples are presented in Fig. 4. All isotherms display a rapid increase in excess adsorption quantity until a peak is reached at pressures of approximately 8–11 MPa and hence show a declining trend at greater pressures. Similar shapes of methane excess adsorption isotherms were also widely reported for many other shales, and the declining trend indicates that the density of methane in free state is approaching the density of adsorbed-phase methane (Rexer et al., 2013; Gasparik et al., 2014; Tian et al., 2016; Li et al., 2017; Zhou et al., 2018).

Table 2 lists the fitting parameters as well as the measured maximum methane excess adsorption capacity (M_{excess}). The M_{excess} values vary between 0.31 cm^3/g rock and 4.08 cm^3/g rock and the fitted n_∞ values range from 0.53 cm^3/g rock to 5.66 cm^3/g rock (Table 2), and the strong correlation between them (Fig. 5a) indicates that the measured M_{excess} values can be treated as a proxy for fitted n_∞ values. The fitted ρ_{ads} values are in the range of 267–523 mg/cm^3, and some of them are greater than the density of liquid methane at its boiling point, e.g., 424 mg/cm^3 (Rexer et al., 2013). Very large densities of adsorbed methane were also reported by other authors when the measured methane excess isotherms do not exhibit maxima or show only an insignificant decline at high pressures (Gasparik et al., 2014; Hu et al., 2015; Tian et al., 2016). In the present study, all isotherms display peak values and significant declines at high pressures, and therefore the presence of very high ρ_{ads} values is probably related to the model itself, and this is beyond the scope of present study. The fitted K_L values range from 0.22 MPa^{-1} to 0.68 MPa^{-1}, which corresponds to a Langmuir pressure (P_L, *the reciprocal of* K_L) range of 1.5–4.6 MPa, values falling into the range of other overmature shales (Wang et al., 2013c; Han et al., 2016; Tian et al., 2016). As illustrated in Fig. 5b, most P_L values range from 1.5 MPa to 2.6 MPa and vary little with TOC values except for two organic-lean samples that have remarkably larger P_L values of 3.6 and 4.5 MPa.

3.3. Methane adsorption at different temperatures

Three samples with different TOC values were selected from Well HY1 for methane excess adsorption measurements at 40, 60, 80, 100 and 120 °C under pressures up to 35 MPa and the measured isotherms are presented in Fig. 6. It is evident that with increasing experimental temperature the peak values of methane excess adsorption isotherms decrease because the methane adsorption process has an exothermic nature (Sircar, 1992), and similar results were also widely observed for many other shales (e.g., Rexer et al., 2013; Gasparik et al., 2014; Tan et al., 2014b; Li et al., 2017, and references therein) and coals (e.g., Hildenbrand et al., 2006).

The measured isotherms were parameterized using three different methods. In Method 1, the adsorption parameters n_∞, K_L and ρ_{ads} are allowed to change with temperature (Rexer et al., 2013; Tian et al., 2016); in Method 2, the n_∞ values keep constant but the other two parameters are temperature-dependent (e.g., Gensterblum et al., 2013); in Method 3, both n_∞ and ρ_{ads} values are fixed and only the K_L values are temperature-dependent (Gasparik et al., 2014; Bruns et al., 2016). All the fitted adsorption parameters are summarized in Table 3, and the fitting results from different methods are presented and compared in Fig. 6. It is visually evident that Methods 1 and 2 yield more satisfactory results than Method 3, particularly in high pressures.

Within the experimental temperature range of 40–120 °C, the n_∞ values fitted with Method 1 decrease with increasing temperature at a rate of 0.024 cm^3/g rock/°C for sample HY1-2, 0.0151 cm^3/g rock/°C for sample HY1-4, and 0.0105 cm^3/g rock/°C for sample HY1-5. These results are similar to the reduction rates of 0.01–0.02 cm^3/g rock/°C for the Lower Cambrian shales from Well FC1 (Li et al., 2017) and other shales (Rexer et al., 2013; Pan et al., 2016). The fitted K_L values are comparable for all the three samples at similar temperatures and they also decrease in similar way with increasing temperature; similarly, the decrease of fitted ρ_{ads} values with increasing temperature is identical for the three samples, with a very narrow range of 0.29–0.44 mg/cm^3/°C.

The respective temperature-independent n_∞ values fitted by the Methods 2 and 3 show only minor differences, e.g., 5.77 cm^3/g rock versus 5.66 cm^3/g rock for sample HY1-2, 3.7 cm^3/g rock versus 3.65 cm^3/g rock for sample HY1-4, and 2.96 cm^3/g rock versus 2.88 cm^3/g rock for sample HY1-5 (Table 3), and these values are close to the average of temperature-dependent n_∞ values determined by Method 1; however, the K_L values by Methods 2 and 3 are higher and decease more

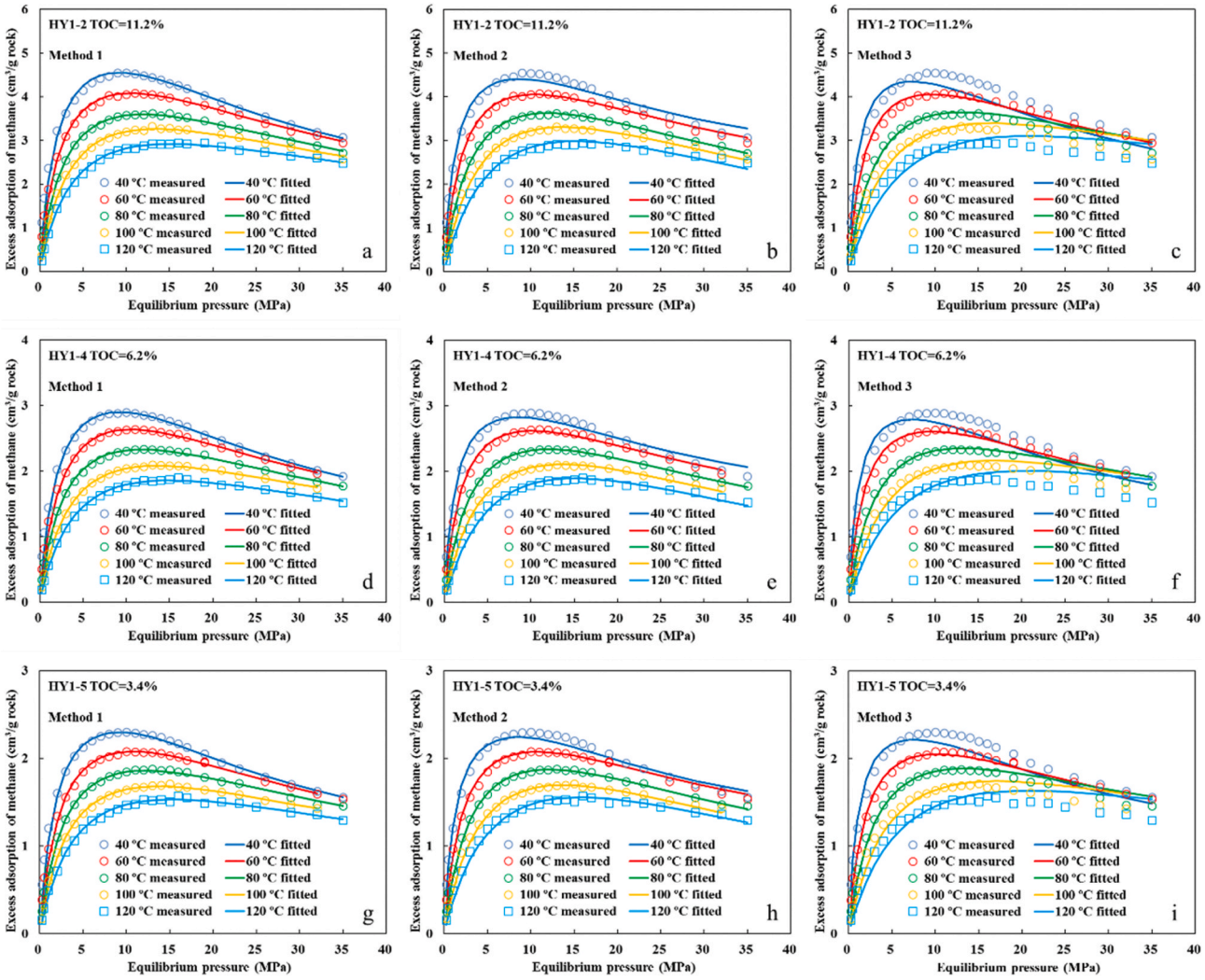

Fig. 6. Plots showing measured and fitted methane excess adsorption isotherms at different temperatures for three selected samples with different TOC values. Method 1 allows all adsorption parameters (n_∞, K_L and ρ_{ads}) to change with temperature, Method 2 keeps the Langmuir volume constant and permits temperature-dependent K_L and ρ_{ads}, while Method 3 only allows K_L to change with temperature.

rapidly than those by Method 1; similarly, a faster decrease of ρ_{ads} values fitted by Method 2 than by Method 1 is also observed with increasing temperature.

4. Discussion

4.1. Main controls on methane adsorption

The relationship between n_∞ values at 60 °C and TOC values is presented in Fig. 7a, and an obvious TOC control on n_∞ values is observed, which is consistent with early studies on other shales (Ross and Bustin, 2009; Zhang et al., 2012; Gasparik et al., 2014). In addition, the regression line in Fig. 7a has a slope of 0.465, indicating an adsorption capacity of organic matters of approximately 46.5 cm^3/g TOC. This value is similar to the values of 40–45 cm^3/g TOC reported for overmature Lower Cambrian shales by other authors (Tan et al., 2014b; Sun et al., 2015; Xia et al., 2015, 2017; Li et al., 2017). The intercept of 0.666 indicates a n_∞ value of 0.666 cm^3/g rock if the sample is free of organic matter (i.e., TOC = 0%), which is close to the n_∞ value of 0.53 cm^3/g rock for the sample YC9-5 that has a TOC value of 0.25% (Table 2).

A close examination of Fig. 7a and Table 2 also reveals a reduction of n_∞ at higher TOC values, and several of them include sample YC9-18 (TOC = 8.52%; n_∞ = 3.73 cm^3/g rock) versus sample YC9-17 (TOC = 7.17%; n_∞ = 4.00 cm^3/g rock), sample YC2-8 (TOC = 4.53%; n_∞ = 1.50 cm^3/g rock) versus sample YC2-2 (TOC = 3.16%; n_∞ = 1.66 cm^3/g rock), and sample HY1-3 (TOC = 5.50%; n_∞ = 3.61 cm^3/g rock) versus sample HY1-6 (TOC = 4.70%; n_∞ = 4.00 cm^3/g rock), and so on. Such a reversal relationship between n_∞ and TOC values is probably related to the different contents of clay minerals among the compared samples. As illustrated in Fig. 7b, the relationships between n_∞ values and total clay contents vary significantly among different sample sets, which indicates on the one hand that the clay mineral may complicate the TOC effect on n_∞ values for some samples and on the other hand that the content of clay minerals is not a robust proxy for the methane adsorption capacity of our samples (Gasparik et al., 2014). Nevertheless, such outlier data for the TOC control on methane adsorption capacity may be smoothed when the dataset is large enough (Sander et al., 2018).

Thermal maturity is also an important control on methane adsorption capacity because higher thermal maturity results in abundant micropores that are the main sites for methane adsorption, especially in the cases of EqVRo <2% (Ross and Bustin, 2009; Mastalerz et al., 2013; Gasparik et al., 2014). Nevertheless, Mastalerz et al. (2013) suggested that the increase of micro- and meso-pore porosity with thermal maturity at EqVRo greater than 2.5% would mitigate or halt. This conclusion is supported by our overmature samples, as evidenced by the strongly

Table 3
Methane adsorption parameters fitted with the Langmuir-based excess adsorption model using different fitting methods. Method 1 allows all parameters to change with temperature; Method 2 has constant n_∞ but varying K_L and ρ_{ads}, while Method 3 has constant n_∞ and ρ_{ads} but varying K_L.

Sample	Temp (°C)	Method 1			Method 2			Method 3		
		n_∞ (cm^3/g rock)	K_L (MPa^{-1})	ρ_{ads} (mg/cm^3)	n_∞ (cm^3/g rock)	K_L (MPa^{-1})	ρ_{ads} (mg/cm^3)	n_∞ (cm^3/g rock)	K_L (MPa^{-1})	ρ_{ads} (mg/cm^3)
HY1-2	40	6.62	0.4586	426	5.77	0.7144	531	5.66	0.8641	446
	60	6.04	0.3838	428	5.77	0.4381	462	5.66	0.5028	446
	80	5.49	0.3134	412	5.77	0.2774	386	5.66	0.2677	446
	100	5.15	0.2557	403	5.77	0.1954	352	5.66	0.1822	446
	120	4.66	0.2220	410	5.77	0.1421	318	5.66	0.1200	446
		$n_\infty = -0.0240 \times T + 7.51$	$K_L = 0.6636 \times \exp(-0.0093 \times T)$	$\rho_{ads} = -0.291 \times T + 439$		$K_L = 1.5057 \times \exp(-0.0202 \times T)$	$\rho_{ads} = -2.684 \times T + 625$		$K_L = 2.2041 \times \exp(-0.0248 \times T)$	
HY1-4	40	4.26	0.4457	418	3.70	0.7186	519	3.65	0.8479	442
	60	3.98	0.3626	413	3.70	0.4602	456	3.65	0.5060	442
	80	3.57	0.3148	406	3.70	0.2792	390	3.65	0.2714	442
	100	3.32	0.2467	401	3.70	0.1925	346	3.65	0.1757	442
	120	3.08	0.2062	380	3.70	0.1392	312	3.65	0.1232	442
		$n_\infty = -0.0151 \times T + 4.85$	$K_L = 0.6565 \times \exp(-0.0096 \times T)$	$\rho_{ads} = -0.442 \times T + 439$		$K_L = 1.5863 \times \exp(-0.0208 \times T)$	$\rho_{ads} = -2.613 \times T + 614$		$K_L = 2.1587 \times \exp(-0.0246 \times T)$	
HY1-5	40	3.31	0.4726	432	2.96	0.7075	506	2.88	0.8450	463
	60	3.09	0.3693	432	2.96	0.4283	471	2.88	0.4698	463
	80	2.83	0.3080	425	2.96	0.2802	395	2.88	0.2784	463
	100	2.64	0.2542	413	2.96	0.1948	353	2.88	0.1815	463
	120	2.49	0.2092	401	2.96	0.1424	334	2.88	0.1309	463
		$n_\infty = -0.0105 \times T + 3.72$	$K_L = 0.6907 \times \exp(-0.0100 \times T)$	$\rho_{ads} = -0.404 \times T + 453$		$K_L = 1.4733 \times \exp(-0.0200 \times T)$	$\rho_{ads} = -2.307 \times T + 596$		$K_L = 1.9812 \times \exp(-0.0234 \times T)$	

positive correlations between TOC and specific micropore volume (V_{DR}) (Fig. 3b), and between fitted n_∞ and V_{DR} (Fig. 8a) for samples of various thermal maturity levels. If thermal maturity still has a significant effect on pore size and methane adsorption capacity of overmature shales, these correlations would become less remarkable than the present observation. It is also worthy to note that the negative intercepts of the regression line in Fig. 8a suggest that there are some pores that are only accessible to CO_2 molecules whose kinetic diameter (0.33 nm) is smaller than that of the methane molecule (0.38 nm). In the case of specific surface area, the S_{BET} values are also positively correlated to TOC values for all samples that have varying thermal maturity levels, although the S_{BET} values for samples from Well HY 1, as a whole, are somewhat larger than other samples at similar TOC values (Fig. 3a). Meanwhile our samples also show a positive correlation between their S_{BET} and n_∞ values with a coefficient of determination of 0.797, but this value becomes larger than 0.9 when regressions were respectively performed on samples of lower (HY1 and YC2 wells) and higher maturity levels (YC9 and FC1 wells) (Fig. 8b). It is worthy to note that the higher maturity samples have larger methane adsorption capacity than lower maturity samples at given specific surface areas, which may indicate that enhanced thermal maturity leads to an increased affinity of pore surface to methane. Nevertheless this speculation has to be further confirmed by more detailed analysis of surface chemistry.

4.2. Fitting method effect on predicted methane adsorption quantity

As mentioned earlier, different fitting methods may yield different adsorption parameters for multi-temperature isotherms, which may lead to some difference when they are extrapolated to geological conditions. Based on the adsorption parameters summarized in Table 3, both the excess and absolute adsorption capacities of samples HY1-2, HY1-4 and HY1-5 were calculated at various temperature and pressure pairs and presented in Fig. 9. The geothermal gradient and surface temperature used in these calculations are 20 °C/km and 15 °C, respectively, and a hydrostatic pressure system is adopted to keep consistent with measured formation pressure coefficients for most of the Lower Cambrian shale system in the study area (Zhang et al., 2015). In the present study, the water in shales is not considered for simplicity and adherence to our experiments, and therefore the methane adsorption quantities of shales discussed below represent the maximum values at subsurface.

From the perspective of gas storage capacity of shales, it has been well recognized that only the excess adsorption capacity is required (Gasparik et al., 2014; Gensterblum et al., 2013; Bruns et al., 2016; Tian et al., 2016). As illustrated in Fig. 9a, c, and e, the predicted profiles of burial depth versus methane excess adsorption are different from each other, particularly in deeper depths when different fitting methods were utilized. For all the three samples, Method 1 always predicts a larger excess adsorption quantity than Methods 2 and 3 at a depth range of 600–1600 m, while all methods yields similar results at the depth range of 1600–3000 m. At depths greater than 3000 m, Method 3 yields methane excess adsorption quantities much larger than Methods 1 and 2, and the latter two methods even predict similar results before the depth of 3800 m, beyond which depth Methods 1 and 2 also begin to yield larger and larger inconsistence (Fig. 9a, c, e). All the results indicate that it makes no significant difference for geological extrapolation within the experimental range of temperature and pressure to adopt fixed or variable Langmuir volume (n_∞) during model fitting, provided that the Langmuir constant (K_L) and adsorbed methane density (ρ_{ads}) are allowed to change with temperature. By contrast, the adoption of fixed n_∞ and ρ_{ads} during model fitting (Method 3) would lead to a much larger methane excess adsorption quantity than Methods 1 and 2, especially beyond the experimental range of temperature and pressure.

The fitting method, however, has a quite different effect on the methane absolute adsorption than the methane excess adsorption (Fig. 9 b, d and e). In particular, methods 2 and 3 produce quite similar results within the investigated range of temperature and pressure, though the two methods have remarkably different ability to fit the measured isotherms (Fig. 7). Moreover, the methane absolute adsorption profile by Method 1 is significantly distinct from those by Method 2, though the two methods yield similar results in the case of methane excess adsorption (Fig. 9 a, c and e). The distinct effects of fitting method on the excess and absolute methane adsorption profiles are related to the remarkably different densities of adsorbed phase methane determined by varying fitting methods (Table 3) that lead to much distinct ratios of

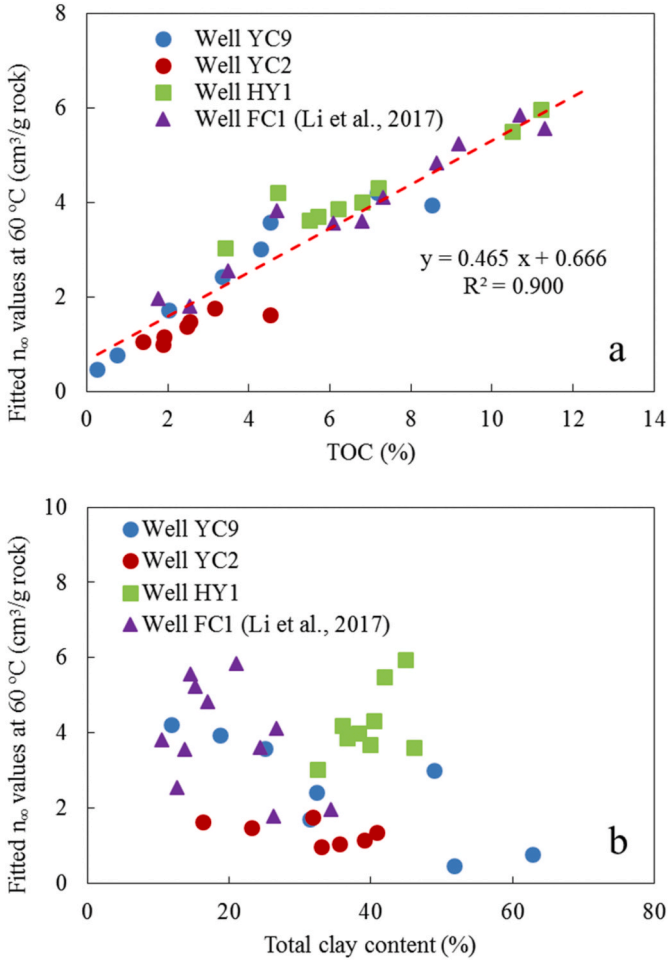

Fig. 7. Plots showing the relationships between fitted n_∞ values and TOC (a) and total clay content (b).

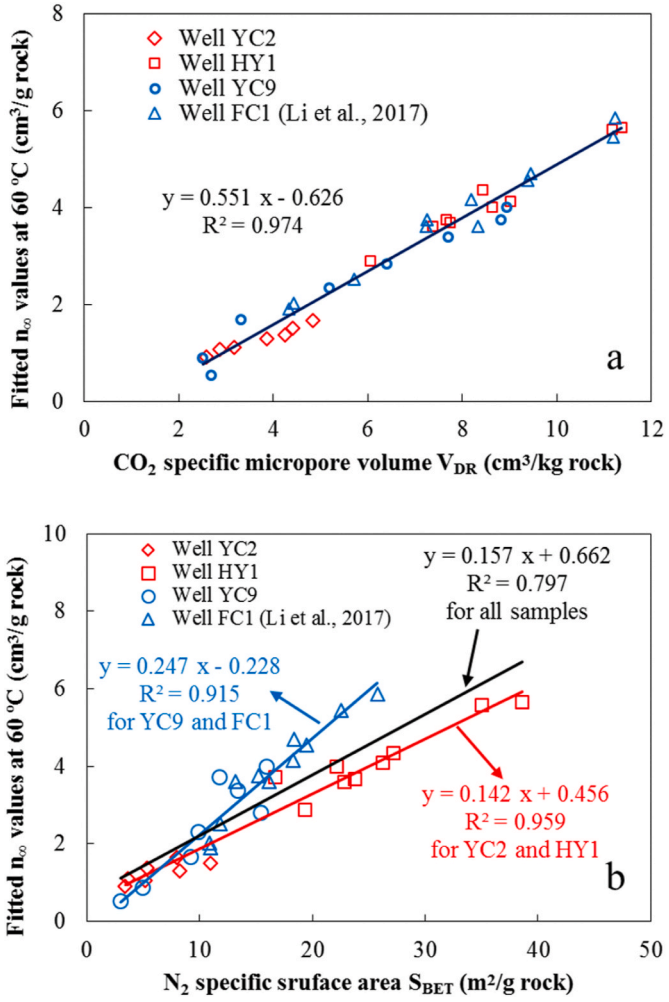

Fig. 8. Plots showing the relationships between fitted n_∞ values and specific micropore volume (a) and specific surface area (b).

ρ_g to ρ_{ads} at deeper depths or greater pressures. Although knowing the methane absolute adsorption quantity is not necessary for the gas-in-place evaluation, it is important for evaluating the relative percentages of adsorbed and free methane and subsequently the flow characteristics of methane during its extraction. In this respect, the adsorbed methane density really matters. Based on the fitting quality of multi-temperature isotherms by the three different methods (Fig. 6), the adoption of constant n_∞ and ρ_{ads} values (Method 3), at least for our isotherms displaying remarkable declining trend in high pressure, is not recommended. Although Methods 1 and 2 are almost equally effective with respect to methane storage evaluation in our experimental range of temperature and pressure, they indeed yield distinct absolute adsorption quantities that subsequently affect the evaluation of relative percentages of adsorbed and free methane. Based on the adsorption data alone, it is currently difficult to discriminate the superiority between Method 1 (varying n_∞) and Method 2 (constant n_∞), which has to be further tested with methane diffusion data in the future.

5. Conclusions

Twenty-four Lower Cambrian shale core samples were collected from three wells in southwest China for geochemical, pore structure and methane adsorption analysis, based on which the following conclusions are summarized:

(1) The investigated samples have a wide span of TOC values ranging from 0.25% to 11.2% and are all overmature with EqVRo values varying between 2.53% and 4.23%; their specific surface areas and micropore volumes respectively determined from subcritical N_2 and CO_2 adsorptions range from 3.0 m^2/g rock to 38.6 m^2/g rock and from 2.5 cm^3/kg rock to 11.4 cm^3/kg rock, both of which have a positive relationship with TOC values.

(2) The positive correlation between TOC and methane adsorption capacity for our samples with a wide span of TOC and EqVRo values confirms that TOC is still a main control on methane adsorption capacity for overmature shales. This also suggests that the effect of thermal maturity variation during the overmature stage (e.g., EqVRo > 2.5%) on methane adsorption capacity may be masked by the strong TOC control. While both specific surface area and micropore volume are positively correlated to methane adsorption capacity, the latter seems to have a stronger control and the specific micropore volume determined from subcritical CO_2 adsorption even can be considered as a proxy for the volume of adsorbed methane in dry shales.

(3) For the Langmuir fitting of methane excess adsorption isotherms at various temperatures, the use of a constant (Method 2) or varying (Method 1) Langmuir volume makes no significant difference with respect to the methane storage capacity of shales when the density of adsorbed methane is allowed to change with temperature. However, the two different methods indeed yield distinct absolute methane adsorption quantities at subsurface, which may lead to remarkably different results for the estimation of relative percentages of adsorbed and free methane.

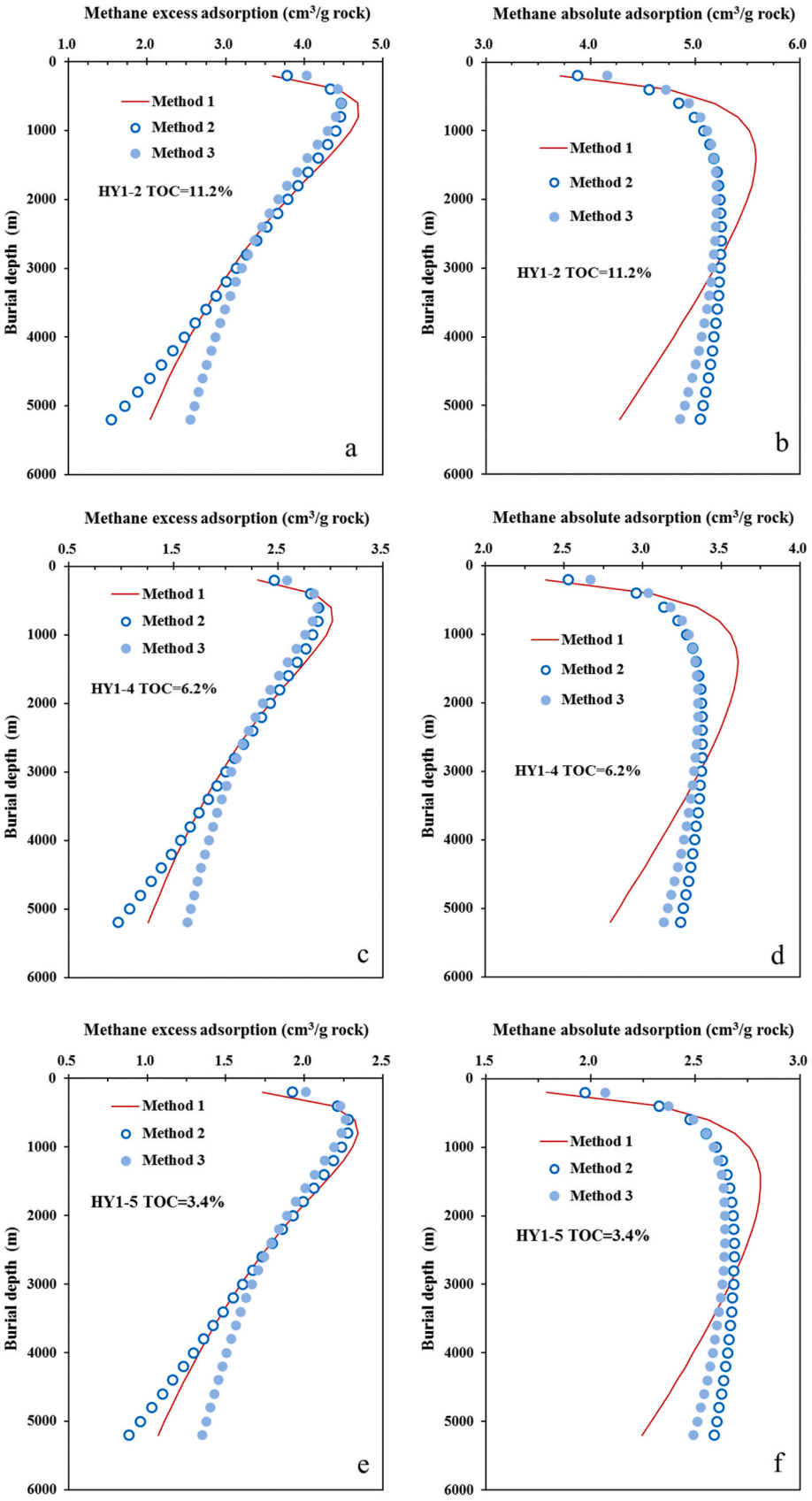

Fig. 9. Changes of predicted methane excess and absolute adsorption quantities with depth for three selected samples using different fitting methods (see details in the text).

Declaration of competing interest

We declare no conflicts of interest, and this manuscript has not been published elsewhere in part or in entirety and is also not under consideration by another journal.

CRediT authorship contribution statement

Haifeng Gai: Data curation, Formal analysis, Writing - original draft. **Tengfei Li:** Data curation, Formal analysis, Writing - original draft. **Xing Wang:** Formal analysis, Visualization. **Hui Tian:** Conceptualization, Validation, Formal analysis, Writing - original draft, Writing - review & editing, Supervision, Project administration, Funding acquisition. **Xianming Xiao:** Formal analysis, Investigation, Validation, Funding acquisition. **Qin Zhou:** Formal analysis, Visualization.

Acknowledgments

This study was jointly supported by the National Natural Science Foundation of China (Grant No. 41925014 and 41522302) and the National Science and Technology Major Project (2017zx05008-002-004). Three anonymous reviewers and the Guest Editors of Max Hu and Jingqiang Tan are thanked for their constructive comments and suggestion, which significantly improved the quality of the original manuscript. This is contribution No.IS-2884 from GIGCAS.

References

Bai, D.Y., Jiang, W., Xiong, X., Zhong, X., 2015. Control of tectonic evolution and tectonic framework on the hydrocarbon accumulation in the western side of the Xuefeng Mountain. Geol. Miner. Resour. South China 31, 199–209 (in Chinese with English abstract).

Bernard, S., Wirth, R., Schreiber, A., Schulz, H.-M., Horsfield, B., 2012. formation of nanoporous pyrobitumen residues during maturation of the Barnett Shale (Fort Worth Basin). Int. J. Coal Geol. 103, 3–11.

Brunauer, S., Emmett, P.H., Teller, E., 1938. Adsorption of gases in multimolecular layers. J. Am. Chem. Soc. 60, 309–319.

Bruns, B., Littke, R., Gasparik, M., van Wees, J.-D., Nelskamp, S., 2016. Thermal evolution and shale gas potential estimation of the Wealden and Posidonia Shale in NW-Germany and The Netherlands: a 3D basin modelling study. Basin Res. 28, 2–33.

Chalmers, G.R.L., Bustin, R.M., 2007. The organic matter distribution and methane capacity of the Lower Cretaceous strata of northeastern British Columbia, Canada. Int. J. Coal Geol. 70, 223–339.

Chalmers, G.R.L., Bustin, R.M., 2017. A multidisciplinary approach in determining the maceral (kerogen type) and mineralogical composition of Upper Cretaceous Eagle Ford Formation: impact on pore development and pore size distribution. Int. J. Coal Geol. 171, 93–110.

Chalmers, G.R.L., Bustin, R.M., 2008. Lower Cretaceous gas shales in northeastern British Columbia, part I: geological controls on methane sorption capacity. Bull. Can. Petrol. Geol. 56, 1–21.

Chen, J., Xiao, M., 2014. Evolution of nanoporosity in organic-rich shales during thermal maturation. Fuel 129, 173–181.

Chen, S., Zhu, Y., Wang, H., Liu, H., Wei, W., Fang, J., 2011. Shale gas reservoir characterization: a typical case in the southern Sichuan Basin of China. Energy 36, 6609–6616.

Curtis, J.B., 2002. Fractured shale-gas systems. AAPG (Am. Assoc. Pet. Geol.) Bull. 86, 1921–1938.

Curtis, M.E., Cardott, B.J., Sondergeld, C.H., Rai, C.S., 2012. Development of organic porosity in the Woodford Shale with increasing thermal maturity. Int. J. Coal Geol. 103, 26–31.

Dai, J., Zou, C., Dong, D., Ni, Y., Wu, W., Gong, D., Wang, Y., Huang, S., Huang, J., Fang, C., Liu, D., 2016. Geochemical characteristics of marine and terrestrial shale gas in China. Mar. Petrol. Geol. 76, 444–463.

De Weireld, G., Frère, M., Jadot, R., 1999. Automated determination of high-temperature and high-pressure gas adsorption isotherms using a magnetic suspension balance. Meas. Sci. Technol. 10, 117–126.

Dreisbach, F., Lösch, H.W., 2002. Highest Pressure adsorption equilibria data: measurement with magnetic suspension balance and analysis with a new adsorbent/adsorbate-volume. Adsorption 8, 95–109.

Fishman, N.S., Hackley, P.C., Lowers, H.A., Hill, R.J., Evenhoff, S.O., Eberl, D.D., Blum, A.E., 2012. The nature of porosity in organic-rich mudstones of the Upper Jurassic Kimmeridge Clay Formation, North Sea, offshore United Kingdom. Int. J. Coal Geol. 103, 32–50.

Furmann, A., Mastalerz, M., Schimmelmann, A., Pedersen, P.K., Bish, D., 2014. Relationships between porosity, organic matter, and mineral matter in mature organic-rich marine mudstones of the Belle Fourche and Second White Specks formations in Alberta, Canada. Mar. Petrol. Geol. 54, 65–81.

Gasparik, M., Bertier, P., Gensterblum, Y., Ghanizadeh, A., Krooss, B.M., Littke, R., 2014. Geological controls on the methane storage capacity in organic-rich shales. Int. J. Coal Geol. 123, 34–51.

Gasparik, M., Ghanizadeh, A., Bertier, P., Gensterblum, Y., Bouw, S., Krooss, B.M., 2012. High-pressure methane sorption isotherms of black shales from The Netherlands. Energy Fuels 26, 4995–5004.

Gensterblum, Y., Merkel, A., Busch, A., Krooss, B.M., 2013. High-pressure CH4 and CO2 sorption isotherms as a function of coal maturity and the influence of moisture. Int. J. Coal Geol. 118, 45–57.

Gregg, S.J., Sing, K.S.W., 1982. Adsorption, Surface Area, and Porosity. Academic Press, New York, p. 303.

Guo, T., Zhang, H., 2014. Formation and enrichment mode of Jiaoshiba shale gas field, Sichuan Basin. Petrol. Explor. Dev. 41, 31–40.

Guo, T., 2013. Evaluation of highly thermally mature shale-Gas reservoirs in complex structural parts of the Sichuan Basin. J. Earth Sci. 24, 863–873.

Han, H., Zhong, N., Ma, Y., Huang, C., Wang, Q., Chen, S., Lu, J., 2016. Gas storage and controlling factors in an over-mature marine shale: a case study of the Lower Cambrian Lujiaping shale in the Dabashan arc-like thrust-fold belt, southwestern China. J. Nat. Gas Sci. Eng. 33, 839–853.

Han, S., Zhang, J., Li, Y., Horsfield, B., Tang, X., Jiang, W., Chen, Q., 2013. Evaluation of lower Cambrian shale in northern Guizhou Province, South China: implications for shale gas potential. Energy Fuels 27, 2933–2941.

Hao, F., Zou, H., Lu, Y., 2013. Mechanisms of shale gas storage: implications for shale gas exploration in China. AAPG (Am. Assoc. Pet. Geol.) Bull. 97, 1325–1346.

Hildenbrand, A., Krooss, B.M., Busch, A., Gaschnitz, R., 2006. Evolution of methane sorption capacity of coal seams as a function of burial history—a case study from the Campine Basin, NE Belgium. Int. J. Coal Geol. 66, 179–203.

Hu, H., Zhang, T., Wiggins-Camacho, J.D., Ellis, G.S., Lewan, M.D., Zhang, X., 2015. Experimental investigation of changes in methane adsorption of bitumen-free Woodford Shale with thermal maturation induced by hydrous pyrolysis. Mar. Petrol. Geol. 59, 114–128.

Jarvie, D.M., 2012. Shale resource systems for oil and gas: part 1—shale-gas resource systems. In: Breyer, J.A. (Ed.), Shale Reservoirs—Giant Resources for the 21st Century, vol. 97. AAPG Memoir, pp. 69–87.

Ji, L., Zhang, T., Milliken, K.L., Qu, J., Zhang, X., 2012. Experimental investigation of main controls to methane adsorption in clay-rich rocks. Appl. Geochem. 27, 2533–2545.

Jin, Z., Firoozabadi, A., 2014. Effect of water on methane and carbon dioxide sorption in clay minerals by Monte Carlo simulations. Fluid Phase Equil. 382, 10–20.

Krooss, B.M., van Bergen, F., Gensterblum, Y., Siemons, N., Pagnier, H.J.M., David, P., 2002. High pressure CH4 and carbon dioxide adsorption on dry and moisture equilibrated Pennsylvanian coals. Int. J. Coal Geol. 51, 69–92.

Leng, J., Gong, D., Li, F., Li, P., 2016. Analysis of the shale gas exploration prospect of the Niutitang Formation in northeastern Guizhou area. Earth Sci. Front. 23, 29–38 (in Chinese with English abstract).

Li, A., Ding, W., He, J., Dai, P., Yin, S., Xie, F., 2016. Investigation of pore structure and fractal characteristics of organic rich shale reservoirs: a case study of Lower Cambrian Qiongzhusi formation in Malong block of eastern Yunnan Province, South China. Mar. Petrol. Geol. 70, 46–57.

Li, T., Tian, H., Xiao, X., Cheng, P., Zhou, Q., Wei, Q., 2017. Geochemical characterization and methane adsorption capacity of overmature organic-rich Lower Cambrian shales in northeast Guizhou region, Southwest China. Mar. Petrol. Geol. 86, 858–873.

Liu, Z., Gao, B., Zhang, Y., Du, W., Feng, D., Nie, H., 2017. Types and Distribution of the Shale Sedimentary Facies of the Lower Cambrian in Upper Yangtze Area, South China. Petroleum Exploration and Development, pp. 21–31.

Littke, R., Cramer, B., Gerling, P., Lopatin, N.V., Poelchau, H.S., Schaefer, R.G., Welte, D. H., 1999. Gas generation and accumulation in the West Siberian Basin. AAPG (Am. Assoc. Pet. Geol.) Bull. 83, 1642–1665.

Loucks, R.G., Reed, R.M., Ruppel, S.C., Jarvie, D.M., 2009. Morphology, genesis, and distribution of nanometer-scale pores in siliceous mudstones of the Mississippian Barnett Shale. J. Sediment. Res. 79, 848–861.

Ma, Y., Zhong, N., Li, D., Pan, Z., Cheng, L., Liu, K., 2015. Organic matter/clay mineral intergranular pores in the Lower Cambrian Lujiaping Shale in the north-eastern part of the upper Yangtze area, China: a possible microscopic mechanism for gas preservation. Int. J. Coal Geol. 137, 38–54.

Mastalerz, M., Schimmelmann, A., Drobniak, A., Chen, Y., 2013. Porosity of Devonian and Mississippian New Albany Shale across a maturation gradient: insights from organic petrology, gas adsorption, and mercury intrusion. AAPG (Am. Assoc. Pet. Geol.) Bull. 97, 1621–1643.

Milliken, K.L., Rudnicki, M., Awwiller, D.N., Zhang, T., 2013. Organic matterehosted pore system, Marcellus Formation (Devonian), Pennsylvania. AAPG Bulletin 97, 177–200.

Montgomery, S.L., Jarvie, D.M., Bowker, K.A., Pollastro, R.M., 2005. Mississippian Barnett Shale, Fort Worth Basin, north-central Texas: gas-shale play with multitrillion cubic foot potential. AAPG (Am. Assoc. Pet. Geol.) Bull. 89, 155–175.

Mosher, K., He, J., Liu, Y., Rupp, E., Wilcox, J., 2013. Molecular simulation of methane adsorption in micro- and mesoporous carbons with applications to coal and gas shale systems. Int. J. Coal Geol. 109 (110), 36–44.

Nie, H., Zhang, J., Li, Y., 2011. Accumulation conditions of the Lower Cambrian shale gas in the Sichuan Basin and its periphery. Acta Pet. Sin. 32, 959–967 (in Chinese with English abstract).

Pan, L., Xiao, X.M., Tian, H., Zhou, Q., Cheng, P., 2016. Geological models of gas in place of the Longmaxi shale in Southeast Chongqing, south China. Mar. Petrol. Geol. 73, 433–444.

Rexer, T.F., Mathia, E.J., Aplin, A.C., Thomas, K.M., 2014. High-pressure methane adsorption and characterization of pores in Posidonia shales and isolated kerogens. Energy Fuels 28, 2886–2901.
Rexer, T.F.T., Benham, M.J., Aplin, A.C., Thomas, K.M., 2013. Methane adsorption on shale under simulated geological temperature and pressure conditions. Energy Fuels 27, 3099–3109.
Ross, D.J.K., Bustin, R.M., 2009. The importance of shale composition and pore structure upon gas storage potential of shale gas reservoirs. Mar. Petrol. Geol. 26, 916–927.
Rouquerol, J., Llewellyn, P., Rouquerol, F., 2007. Is the BET equation applicable to microporous adsorbents? Stud. Surf. Sci. Catal. 160, 49–56.
Sander, R., Pan, Z., Connell, K.D., Camilleri, M., Grigore, M., Yang, Y., 2018. Controls on methane sorption capacity of Mesoproterozoic gas shales from the Beetaloo Sub-basin, Australia and global shales. Int. J. Coal Geol. 199, 65–90.
Schoenherr, J., Littke, R., Urai, J.L., Kukla, P.A., Rawahi, Z., 2007. Polyphase thermal evolution in the Infra-Cambrian Ara group (South Oman salt basin) as deduced by maturity of solid reservoir bitumen. Org. Geochem. 38, 1293–1318.
Sircar, S., 1992. Estimation of isosteric heats of adsorption of single gas and multicomponent gas mixtures. Ind. Eng. Chem. Res. 31, 1813–1819.
Sun, M., Yu, B., Chen, S., Xia, W., Ye, R., 2015. Reservoir characteristics and adsorption capacity of the Lower Cambrian Niutitang Formation shale in the southeast of Chongqing: a case study of well Yuke 1 and well Youke 1. J. Northeast Petrol. Univ. 39, 69–79 (in Chinese with English abstract).
Tan, J., Horsfield, B., Fink, R., Krooss, B., Schulz, H.-M., Rybacki, E., Zhang, J., Boreham, C.J., van Graas, G., Tocher, B.A., 2014a. Shale gas potential of the major marine shale formations in the Upper Yangtze Platform, South China, part III: mineralogical, lithofacial, petrophysical, and rock mechanical properties. Energy Fuels 28, 2322–2342.
Tan, J., Weniger, P., Krooss, B.K., Merkel, A., Horsfield, B., Zhang, J., Boreham, C.J., van Graas, G., Tocher, B.A., 2014b. Shale gas potential of the major marine shale formations in the Upper Yangtze Platform, South China, part II: methane sorption capacity. Fuel 129, 204–218.
Tian, H., Li, T., Zhang, T., Xiao, X., 2016. Characterization of methane adsorption on overmature Lower Silurian–Upper Ordovician shales in Sichuan Basin, southwest China: experimental results and geological implications. Int. J. Coal Geol. 156, 36–49.
Tian, H., Pan, L., Xiao, X.M., Wilkins, R.W.T., Meng, Z.P., Huang, B.J., 2013. A preliminary study on the pore characterization of Lower Silurian black shales in the Chuandong Thrust Fold Belt, Southwestern China using low pressure N_2 adsorption and FE-SEM methods. Mar. Petrol. Geol. 48, 8–19.
Tian, H., Pan, L., Zhang, T., Xiao, X., Meng, Z., Huang, B., 2015. Pore characterization of organic-rich Lower Cambrian shales in Qiannan depression of Guizhou Province, Southwestern China. Mar. Petrol. Geol. 62, 28–43.
Topór, T., Derkowski, A., Ziemiański, P., Szczurowski, J., McCarty, D.K., 2017. The effect of organic matter maturation and porosity evolution on methane storage potential in the Baltic Basin (Poland) shale-gas reservoir. Int. J. Coal Geol. 180, 46–56.
Wang, F., Guan, J., Feng, W., Bao, L., 2013a. Evolution of overmature marine shale porosity and implication to the free gas volume. Petrol. Explor. Dev. 40, 819–824.
Wang, L.B., Jiu, K., Zeng, W.T., Fu, J.L., Zhao, S., 2013b. Characteristics of Lower Cambrian marine black shales and evaluation of shale gas prospective area in Qianbei area, Upper Yangtze region. Acta Petrol. Sin. 29, 3263–3278.
Wang, S., Song, Z., Cao, T., Song, X., 2013c. The methane sorption capacity of Paleozoic shales from the Sichuan Basin, China. Mar. Petrol. Geol. 44, 112–119.
Wang, Z., Xie, Y., Yang, P., Zhuo, J., He, J., Xie, S., 2012. Marine basin evolution and oil and gas geology of Sinian-early Paleozoic period on the western side of the Xuefeng Mountain. Geol. Bull. China 31, 1795–1811 (in Chinese with English abstract).
Weishauptová, Z., Přibyl, O., Sýkorová, I., René, M., 2017. Effect of the properties of Silurian shales from the Barrandian Basin on their methane sorption potential. Fuel 203, 68–81.
Weniger, P., Kalkreuth, W., Busch, A., Krooss, B.M., 2010. High-pressure methane and carbon dioxide sorption on coal and shale samples from the Paraná Basin, Brazil. Int. J. Coal Geol. 84, 190–205.
Wignall, P.B., Newton, R., 1998. Pyrite framboid diameter as a measure of oxygen deficiency in ancient mudrocks. Am. J. Sci. 298, 537–552.
Xia, J., Wang, S., Cao, T., Yang, J., Song, Z., 2015. The characteristics of pore structure and its gas storage capacity of the Lower Cambrian shales from the northern Guizhou Province. Nat. Gas Geosci. 26, 1744–1754 (in Chinese with English abstract).
Xia, J., Song, Z., Wang, S., Zeng, W., 2017. Preliminary study of pore structure and methane sorption capacity of the Lower Cambrian shales from the north Guizhou Province. J. Nat. Gas Sci. Eng. 38, 81–93.
Yang, F., Ning, Z., Zhang, R., Zhao, H., Krooss, B.M., 2015. Investigations on the methane sorption capacity of marine shales from Sichuan Basin, China. Int. J. Coal Geol. 146, 104–117.
Zhang, T.W., Ellis, G.S., Rupple, S.C., Milliken, K., Yang, R., 2012. Effect of organic matter type and thermal maturity on methane adsorption in shale-gas systems. Org. Geochem. 47, 120–131.
Zhang, Z., Cheng, L., Zeng, C., 2015. Geological characteristics and exploration prospect of Lower Cambrian Niutitang shale gas in Suiyang area, Guizhou. Mar. Orig. Pet. Geol. 20, 39–42 (in Chinese with English abstract).
Zhou, S., Xue, H., Ning, Y., Guo, W., Zhang, Q., 2018. Experimental study of supercritical methane adsorption in Longmaxi shale: insights into the density of adsorbed methane. Fuel 211, 140–148.